Atomic-resolution imaging of lithium in Al_3Li precipitates

M. D. Rossell,[1] R. Erni,[1] M. Asta,[2] V. Radmilovic,[1] and U. Dahmen[1]
[1]*National Center for Electron Microscopy, Lawrence Berkeley National Laboratory, Berkeley, California 94720, USA*
[2]*Department of Chemical Engineering and Materials Science, University of California–Davis, Davis, California 95616, USA*
(Received 1 May 2009; revised manuscript received 11 June 2009; published 13 July 2009)

Using an aberration-corrected transmission electron microscope, we report on imaging individual atomic columns of Li in the intermetallic compound Al_3Li. The effect of electron energy on the imaging characteristic of Li is investigated by performing measurements at 80 kV employing a monochromated electron beam with an energy spread ΔE of 0.2 eV and at 300 kV with ΔE of 0.8 eV. These settings enable similar information transfer at both microscope operation conditions and allow a direct comparison between the 80 and the 300 kV measurements. Our experimental data show that the phase of the reconstructed exit-plane wave is highly sensitive to light atoms and that the displacement damage of light elements of low threshold recoil energy can be larger at 80 kV than at 300 kV. This behavior can be understood in terms of the relativistic elastic-scattering cross section between electrons and atoms.

DOI: 10.1103/PhysRevB.80.024110 PACS number(s): 81.40.Wx, 68.37.Og, 75.20.En

I. INTRODUCTION

Al-Li alloys are of great interest for aerospace[1] and cryogenic[2] applications due to their low density and high strength-to-weight ratio. The mechanical properties of these alloys are based on a fine dispersion of coherent Al_3Li metastable precipitates formed by congruent ordering and spinodal decomposition.[3] Other elements, such as Sc and Zr, are added to Al-Li alloys to further improve their properties. These alloys were found to contain a fine distribution of remarkably monodisperse core/shell precipitates consisting of an $Al_3(ScLi)$ core surrounded by a shell of pure Al_3Li, with Zr segregating at the core/shell interface.[4] Similar core/shell precipitates in Al-Li-Sc alloys have been shown to increase hardness.[5] Optimizing the performance of such alloys requires an understanding of Li partitioning in these complex precipitates because Li-atom positions are closely linked to the electronic structure of precipitates and consequently the alloy's physical properties.[6] However, direct imaging of atomic columns of light elements, particularly when surrounded by heavier elements, has been challenging. Li is the lightest solid element, implying a very weak electron-scattering power. Hence, due to the limited sensitivity and resolution of conventional transmission electron microscopes, extensive data analysis is required to detect light elements such as Li.[7] In this contribution, we report on imaging of Li-atom columns in Al_3Li by employing an aberration-corrected transmission electron microscope[8] that provides the enhanced sensitivity and resolution necessary for imaging of light elements.[9,10]

II. METHODS

A. Experiment

The TEAM 0.5 transmission electron microscope is equipped with a hexapole-type imaging-aberration corrector and a monochromated high-brightness gun. A detailed description of the instrument and its capabilities is given in Ref. 11. The aberration corrector was fine tuned at accelerating voltages of 80 and 300 kV. After fine tuning of the aberration corrector at 80 kV, the following aberration coefficients were measured (for nomenclature see, e.g., Ref. 12): A_2=29 nm, B_2=24 nm, C_3=−3 μm, A_3=429 nm, S_3=435 nm, A_4=15 μm, D_4=10.5 μm, B_4=11.6 μm, C_5=6 mm, and A_5=279 μm. However, for a chromatic aberration coefficient C_C of 1.1 mm (at 80 kV) and a characteristic energy spread of ~0.8 eV, the information transfer at 80 kV is severely limited by partial temporal coherence. We therefore employed the monochromator to reduce the inherent energy spread of the electron beam to ΔE =0.22 eV, thereby increasing the information limit at 80 kV from 0.175 to 0.092 nm. At 300 kV, a comparable information limit of 0.086 nm is obtained with a nonmonochromated electron beam of 0.8 eV energy spread and a C_C of 2.1 mm. The following aberration coefficients were measured at 300 kV: A_2=20 nm, B_2=32 nm, C_3=−13 nm, A_3=2.4 nm, S_3=1141 nm, A_4=36 μm, D_4=14.2 μm, B_4=10.4 μm, C_5=5.2 mm, and A_5=1.7 mm. The aberration coefficients are given here without azimuth angles. Defocus C_1 and twofold astigmatism A_1 were manually optimized. The two-dimensional (2D) contrast-transfer functions (CTFs) calculated for both acceleration voltages on the basis of the aberration coefficients mentioned above are depicted in Fig. 1. For an aberration-corrected instrument, it is essentially the information limit due to partial temporal coherence that imposes the limit on the information transfer of high spatial frequency components of the exit-plane wave (EPW) to the image intensity. Hence, the above values reflect the information limits due to partial temporal coherence and were determined by using the known expressions which, e.g., can be found in Ref. 13. Fluctuations of the lens currents and the high-tension ripple were neglected. White circles indicate the microscope information limit at 300 [Fig. 1(a)] and 80 kV [Fig. 1(b)] revealing that similar information transfer is obtained in both modes.

The alloy was synthesized as described in Ref. 4 and transmission electron microscopy (TEM) samples were prepared using conventional electropolishing methods. The specimen consisted of a polycrystalline Al-rich matrix containing $Al_3(Li,Sc,Zr)$ core/shell precipitates. Figure 2(a) shows a dark field image of the sample recorded using a 110

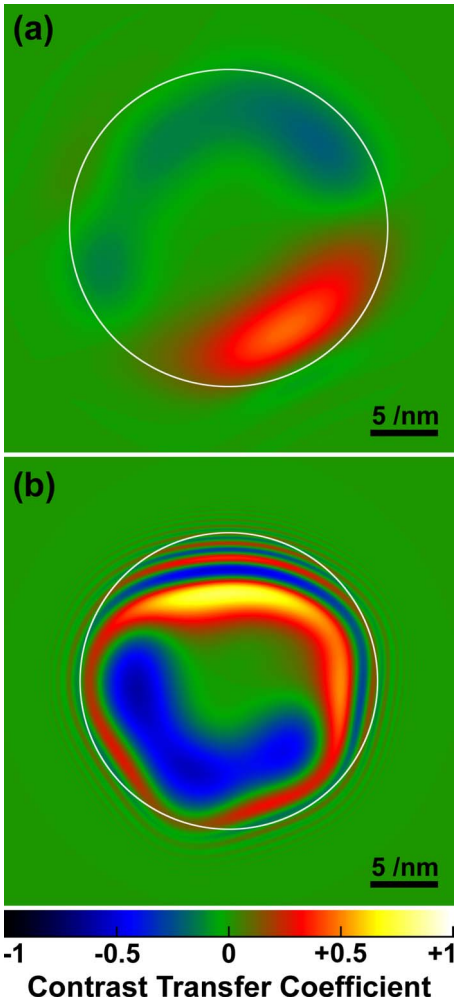

FIG. 1. (Color online) CTFs calculated from the measured residual aberrations obtained at (a) 300 and (b) 80 kV employing a quasimonochromatic electron beam. The microscope information limit, indicated by white circles, is 0.086 and 0.092 nm, respectively. Defocus C_1 and twofold astigmatism A_1 are set at zero.

superlattice reflection. In a 2D projection, the precipitates exhibit a doughnut shape with a bright shell of Al_3Li surrounding a core region whose contrast closely resembles the Al matrix. The ordered Al_3Li phase has the $L1_2$ structure [Fig. 2(b)] and is fully coherent with the fcc Al matrix. The lattice parameters are a_{cub}=0.401 nm and the projection along the [001] zone axis exhibits Li- and Al-atom columns separated by 0.2 nm.

B. First-principles calculations

As discussed below, Al_3Li was observed to undergo radiation damage displaying an anomalous dependence on incident electron energy. To determine the origin of this behavior, values of the threshold recoil energies ($T_{d,\min}$) for Al and Li atoms in Al_3Li were required, which are presently unavailable in the literature. First-principles calculations, based on the framework of electronic density-functional theory (DFT), were thus undertaken to provide estimates of $T_{d,\min}$ in this compound.

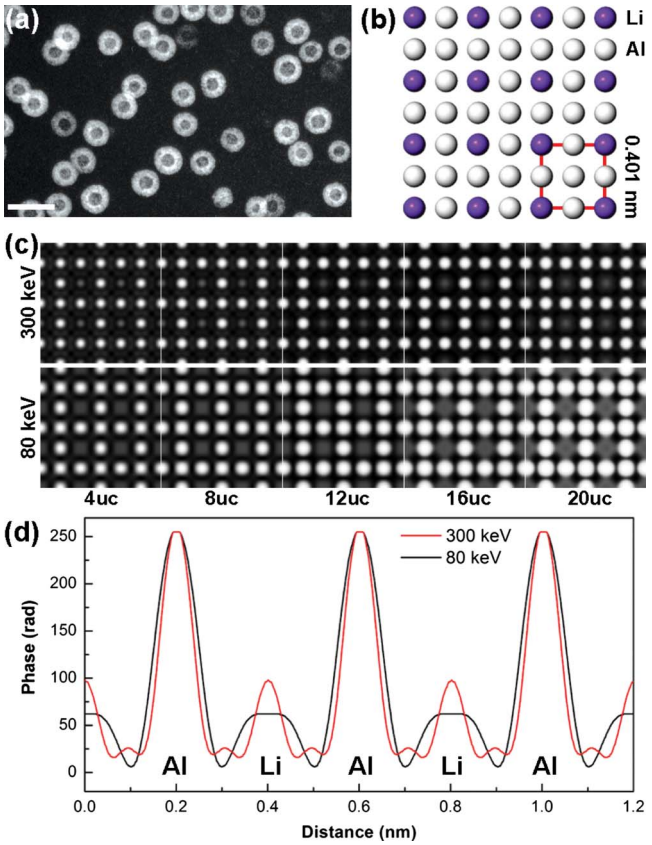

FIG. 2. (Color online) (a) Dark field image of an AlLiScZr alloy recorded using the 110 superlattice reflection. Scale bar is 50 nm. (b) Model of the $L1_2$ structure of fully ordered Al_3Li. The lattice parameter is a=0.401 nm. The projection of a 3×3 unit cell along the [001] zone axis shows Li- and Al-atom columns separated by 0.2 nm. (c) Al_3Li EPW phase images simulated in the [001] zone axis for 300 (upper row) and 80 kV (bottom row) for increasing specimen thickness (marked in multiples of unit cells of 0.401 nm). (d) Corresponding single-pixel line profiles across the calculated EPW phase images for a specimen thickness of 4 unit cells (4 uc).

The most direct approach for calculating $T_{d,\min}$ is through the application of nonequilibrium molecular-dynamics (MD) simulations. This approach is exemplified by the work of Refs. 14 and 15, where classical interatomic potentials were employed in MD calculations of $T_{d,\min}$ for $L1_2$ Cu_3Au and Ni_3Al. In the present work, DFT was chosen as the basis for the energy calculations, rather than classical interatomic potential models, to ensure an accurate description of alloy chemistry. Due to the high computational cost of DFT, relative to classical potentials, estimates of $T_{d,\min}$ were derived employing a more efficient approach based on the so-called "sudden approximation" (SA) rather than full MD simulations. Within the SA approach, $T_{d,\min}$ is derived by calculating the energy barrier encountered as an atom is displaced from its binding site to a neighboring interstitial location, holding the positions of all other atoms fixed. As discussed in a recent study,[16] in cases where results of MD and SA calculations have been compared, values for $T_{d,\min}$ are found to agree to within approximately 10%.

The SA is only appropriate for estimating $T_{d,\min}$ along directions where there is an unobstructed path from an at-

om's binding site to a neighboring interstitial position. In the current work, $T_{d,\min}$ was calculated along the ⟨111⟩ crystallographic direction. In previous studies of $L1_2$ Ni_3Al and Cu_3Au, $T_{d,\min}$ along the ⟨111⟩ direction has been shown to be significantly larger (by approximately 50%) than the value corresponding to the ⟨100⟩ direction relevant to the present experimental work. Thus, the calculated results obtained here are considered as upper bounds for $T_{d,\min}$ under the relevant experimental conditions.

The SA calculations made use of 108-atom supercells ($3\times3\times3$ unit $L1_2$ cells), and were performed using the *ab initio* total-energy and molecular-dynamics program Vienna *ab initio* simulation program (VASP) developed at the Institut für Materialphysik, Universität Wien.[17–19] These calculations made use of the Perdew-Burke-Ernzerhof generalized-gradient approximation[20] and the projector augmented wave formalism,[21,22] employing the Al and Li potentials labeled "Al" and "Li_sv" in the VASP library. The calculations employed $5\times5\times5$ *k*-point meshes in the reducible zone and a plane-wave cutoff of 350 eV; with these settings the energies were estimated to be converged to within approximately 0.075 eV for the 108-atom supercells. Calculations were performed considering Al or Li atoms at 10 positions spanning a displacement of [0.5, 0.5, 0.5] in units of the $L1_2$ unit-cell lattice constant. From the maximum value of the energy along this path, we obtained estimates for $T_{d,\min}$ of 18 eV for Al and 9.5 eV for Li in Al_3Li.

III. RESULTS

A. Calculated exit-plane wave functions

By performing calculations of the EPW based on the multislice algorithm,[23] we investigated the dependence of the imaging characteristic of Al_3Li on the accelerating voltage. Figure 2(c) shows a series of images illustrating the phase of the calculated EPWs for a thickness range of 4–20 unit cells (1.6–8.0 nm) along the Al_3Li [001] zone axis. The top row in Fig. 2(c) was calculated for an accelerating voltage of 300 kV and the bottom row for 80 kV. The corresponding single-pixel line profiles across the calculated EPW phase images for a specimen thickness of 4 unit cells are shown in Fig. 2(d). For thin specimens the phase of the EPW is proportional to the projected atomic number of the atom column in the direction of the incident electron beam. The simulations in Fig. 2(c) show strong peaks at Al positions and weaker peaks at Li positions. With increasing specimen thickness and decreasing accelerating voltage, the width of the phase peaks spreads due to the increased dynamic behavior of the elastic electron scattering.

It can be argued that the presence of peaks at the Li positions in the phase images are due to dynamical diffraction effects. However, simulations equivalent to Fig. 2(c) (not shown) with the Li columns removed revealed that dynamical diffraction effects do not lead to the formation of maxima at the Li positions. Hence, it is the presence of Li that causes the maxima in the phase images in Fig. 2(c).

B. Experimental exit-plane wave functions

Figure 3 shows EPW phase images of the Al_3Li shell for 300 and 80 kV, respectively. These images were retrieved from 20-member focal series of images. The particles selected were located at the very edge of the TEM foil, where the thickness was below 10 nm—only 1/3 of the precipitate diameter. This sample geometry corresponds to a cross section of the particle so that no overlap with the Al matrix is expected and pure Li columns can be imaged. The image series used focal steps of 1.6 nm at 300 kV and 0.9 nm at 80 kV. For a current density of 7.9 A/cm^2 at 300 kV and 44.4 A/cm^2 at 80 kV, respectively, the exposure times were 1 s at 300 kV and 0.5 s at 80 kV. The phase images in Fig. 3

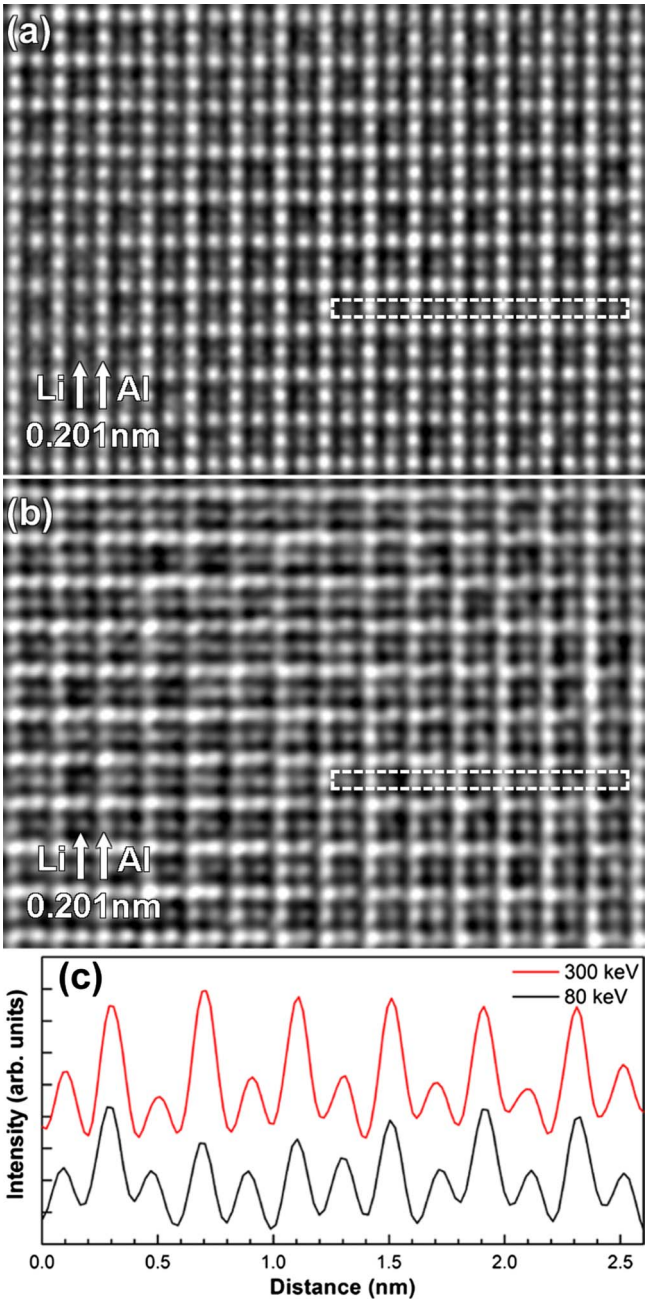

FIG. 3. (Color online) Al_3Li EPW phase images retrieved from 20 experimental images obtained at (a) 300 and (b) 80 kV using a monochromator. (c) Single-pixel line profiles across the atom rows marked with white rectangles in the experimental images.

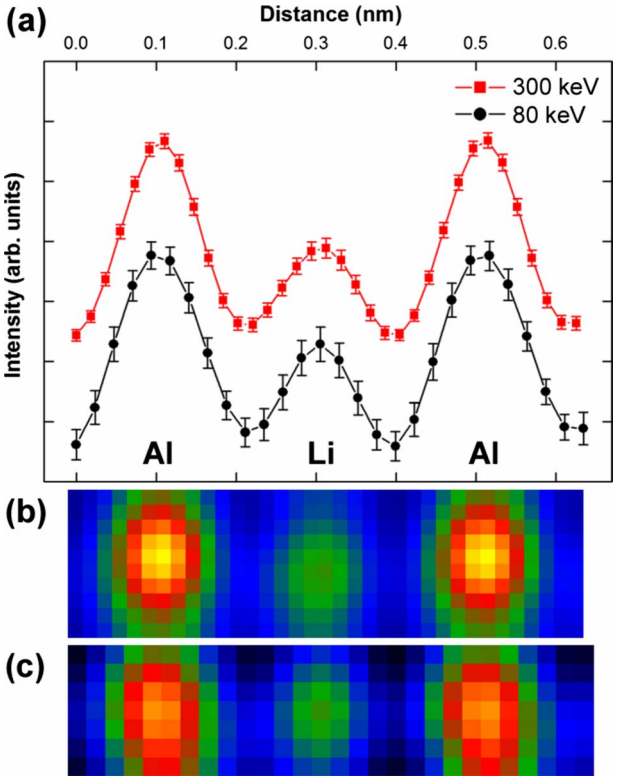

FIG. 4. (Color online) (a) Single-pixel line profiles across the averaged structures (b and c) derived from an area containing 100 unit cells in Figs. 3(a) and 3(b), respectively. A sampling of 0.0184 and 0.0235 nm/pixel was used at 300 and 80 kV, respectively.

show Li-atom columns clearly resolved next to Al-atom columns. Figure 3(c) shows single-pixel line profiles across the atom rows marked by rectangles in Figs. 3(a) and 3(b), revealing a random intensity variation between unit cells, which is particularly pronounced at 80 kV. The results of the simulations support that the phase maxima at the Li positions reflect the presence of Li and are not due to dynamical diffraction effects.

For a statistical assessment of the Li signal, we derived averaged structures from the experimental phase images in Figs. 3(a) and 3(b) of areas containing 10×10 unit cells. These averaged structures and the corresponding single-pixel line profiles for the experimental-phase images are shown in Fig. 4. The error bars in the line profiles are the standard deviations obtained by comparing the individual peaks with the averaged structure.

IV. DISCUSSION

From Figs. 3 and 4, it can be concluded that for both accelerating voltages, the Li is resolved with a signal that significantly exceeds the noise level. As seen in Fig. 4(a), the signal-to-noise ratio for the Li phase peak is 5.8 at 300 kV and 3.3 at 80 kV. Although the intensity of the Li columns is weaker than the neighboring Al columns at both accelerating voltages, the Al/Li intensity ratio is markedly smaller at 80 kV than at 300 kV, in contradiction with the prediction based on the multislice simulations; see Fig. 2(d). Figures 3 and 4

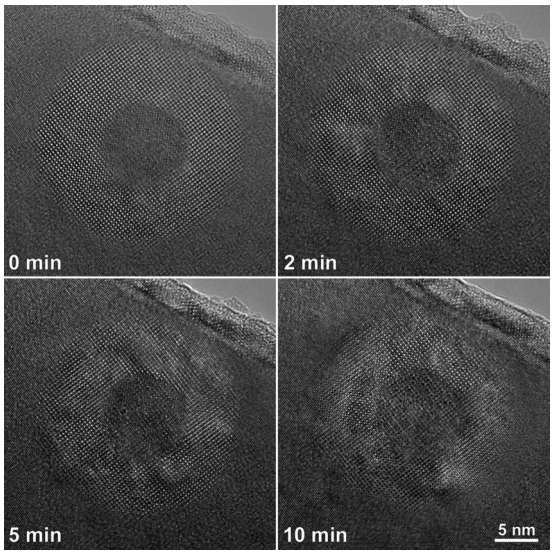

FIG. 5. Sequence of HRTEM images of a core/shell particle showing the effect of electron radiation after 0, 2, 5, and 10 min of exposure with an 80 kV electron beam. The current density used was similar to the one used to record the focal series at 80 kV.

reveal that at 80 kV, the chemical contrast is reduced and local intensity variations strongly affect the Li signal. This is supported by the standard deviations of the line profiles, which are about twice as large at the lower voltage. Furthermore, the 80 kV line profile in Fig. 3(c) shows larger intensity variations between equivalent atomic columns. These variations are due to unexpectedly strong radiation effects.

In Fig. 5, a sequence of high-resolution transmission electron microscopy (HRTEM) images of a core/shell particle shows the effect of electron irradiation after an exposure of 0, 2, 5, and 10 min to an 80 kV electron beam. Note that after 2 min, the incident radiation causes structural changes in the Al_3Li shell resulting in local residual mistilts such as those observed in the 80 kV phase image of Fig. 3(b). Meanwhile, the Al matrix is unaffected by radiation damage even after 10 min of electron exposure.

To understand this anomalous behavior, we calculated total scattering cross sections based on the relativistic differential scattering cross sections of McKinley and Feshbach.[24] By integration over the solid angle (see, e.g., Ref. 25), we obtain the total scattering cross section for atom displacement σ_d as a function of electron energy

$$\sigma_d = 10^{-4}\pi\frac{\mathrm{kg}^2\,\mathrm{m}^2}{\mathrm{C}^4}\frac{e^4}{m_e^2}Z^2\frac{(1-\beta^2)}{\beta^4} \times\left[(\kappa-1)-\beta^2\ln\kappa+\pi\frac{Z}{137}\beta(2\sqrt{\kappa}-2-\ln\kappa)\right], \quad (1)$$

where e is the elementary charge, m_e the rest mass of the electron, Z the atomic number, and $\beta=\frac{v_e}{c}$, with v_e the relativistic speed of the electron for an electron energy eU, with U the acceleration potential of the microscope, and c is the speed of light in vacuum. The factor $\kappa=\frac{T_{\max}}{T_{d,\min}}$ denotes the

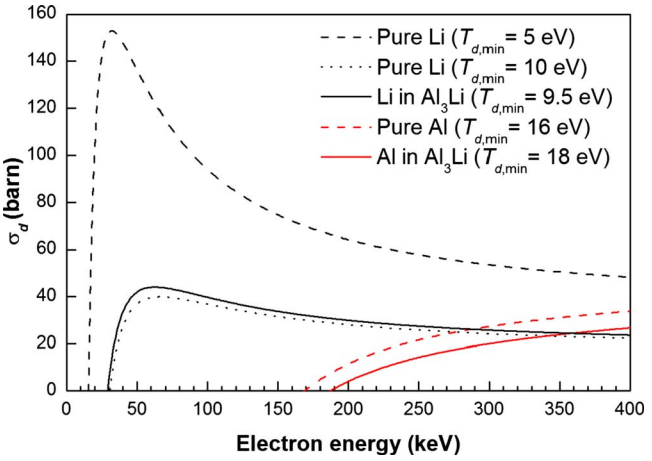

FIG. 6. (Color online) Total scattering cross section σ_d for atom displacement for Al and Li as a function of the primary electron energy.

ratio between the maximum recoil energy $T_{\max}$, i.e., the maximum energy that an electron with a kinetic energy eU can transfer to an atom of mass m_{atom}, and the minimum threshold recoil energy $T_{d,\min}$, i.e., the critical recoil energy to initiate atom displacement. The maximum recoil energy is given by

$$T_{\max} = 4\frac{m_e}{m_{\text{atom}}}eU\left(1 + \frac{eU}{2m_e c^2}\right). \quad (2)$$

Using expression (1) with the estimates for $T_{d,\min}$ derived from the first-principles calculations described in Sec. II B, we plotted the total scattering cross section for atom displacement σ_d vs energy for Al and Li in Al_3Li (Fig. 6). We find that for Al, σ_d decreases monotonically with decreasing electron energy and vanishes at ~190 kV.

By contrast, Li displays an anomalous behavior; the displacement scattering cross section reaches a maximum at ~60 kV and decreases with increasing electron energy thus making Al_3Li more susceptible to radiation damage at 80 kV than at 300 kV. As discussed in Sec. II B, the estimated $T_{d,\min}$ values for Al and Li atoms in Al_3Li are calculated along the ⟨111⟩ direction and likely overestimate the value of $T_{d,\min}$ for the ⟨100⟩ direction relevant to the present experimental work. Nevertheless, the predicted anomalous energy dependence on incident electron energy for Li also holds at lower values of $T_{d,\min}$ as shown in Fig. 6. Similar results are obtained for pure Al and Li. The average threshold recoil energy for pure Al is 16 eV,[26] while for pure Li $T_{d,\min}$ is estimated to be between 5 and 10 eV.[27] For pure Al, the creation of point defects through knock-on radiation damage is possible at 300 kV but not at 80 kV. This is consistent with the observation in Fig. 5 that at 80 kV the radiation damage is confined to the Al_3Li precipitates without affecting the surrounding Al matrix.

V. CONCLUSION

We conclude that atomic columns of Li in the intermetallic phase Al_3Li can be imaged at 300 and 80 kV. By employing a monochromator in the case of the 80 kV measurement, for both operation conditions a comparable information transfer of ~0.09 nm was achieved. Our results of imaging Li columns at 80 kV uncover an unexpected increased susceptibility to knock-on radiation damage of light elements at lower accelerating voltages. This observation places important boundary conditions on electron microscopy observations of light elements even beyond Li. It is evident that in the tunable operating range of the instrument between ~60 and 300 kV, and for a realistic range of binding energies, Li, Be, and even B can be susceptible to the same anomaly. Strategies to avoid this effect or to utilize it as a means of selectively affecting specific atomic sites are readily apparent. For the case of Al_3Li investigated here, the damage can be minimized by using electron energies below the peak in the scattering cross section while employing a monochromated electron beam to maintain image resolution or by using nonmonochromated higher electron energies at lower electron flux.

ACKNOWLEDGMENTS

This work was supported by the Director, Office of Science, Office of Basic Energy Sciences, Materials Sciences and Engineering Division, of the (U.S.) Department of Energy under Contract No. DE-AC02-05CH11231. This work was performed at the National Center for Electron Microscopy under the TEAM project, which is supported by the Department of Energy, Office of Science, Office of Basic Energy Sciences. M.A. acknowledges funding from the Department of Energy, Office of Basic Energy Sciences under Grant No. DE-FG02-06ER46282. We acknowledge C. Kisielowski for help with the retrieval of the exit-plane waves and the statistical assessment of the Li signal.

[1] J. W. Martin, Annu. Rev. Mater. Sci. **18**, 101 (1988).
[2] K. T. V. Rao and R. O. Ritchie, Acta Metall. Mater. **38**, 2309 (1990).
[3] V. Radmilovic, A. G. Fox, and G. Thomas, Acta Metall. **37**, 2385 (1989).
[4] V. Radmilovic, A. Tolley, E. A. Marquis, M. D. Rossell, Z. Lee, and U. Dahmen, Scr. Mater. **58**, 529 (2008).
[5] M. E. Krug, D. C. Dunand, and D. N. Seidman, Appl. Phys. Lett. **92**, 124107 (2008).
[6] A. Arya, G. P. Das, H. G. Salunke, and S. Banerjee, J. Phys.: Condens. Matter **6**, 3389 (1994).
[7] Y. Shao-Horn, L. Croguennec, C. Delmas, E. C. Nelson, and M. A. O'Keefe, Nature Mater. **2**, 464 (2003).
[8] The Transmission Electron Aberration-corrected Microscope (TEAM) project is supported by the Department of Energy, Office of Science, Basic Energy Sciences.

[9] J. C. Meyer, C. Kisielowski, R. Erni, M. D. Rossell, M. F. Crommie, and A. Zettl, Nano Lett. **8**, 3582 (2008).
[10] Ç. Ö. Girit, J. C. Meyer, R. Erni, M. D. Rossell, C. Kisielowski, L. Yang, C.-H. Park, M. F. Crommie, M. L. Cohen, S. G. Louie, and A. Zettl, Science **323**, 1705 (2009).
[11] C. Kisielowski, B. Freitag, M. Bischoff, H. van Lin, S. Lazar, G. Knippels, P. Tiemeijer, M. van der Stam, S. von Harrach, M. Stekelenburg, M. Haider, S. Uhlemann, H. Müller, P. Hartel, B. Kabius, D. Miller, I. Petrov, E. A. Olson, T. Donchev, E. A. Kenik, A. R. Lupini, J. Bentley, S. J. Pennycook, I. M. Anderson, A. M. Minor, A. K. Schmid, T. Duden, V. Radmilovic, Q. M. Ramasse, M. Watanabe, R. Erni, E. A. Stach, P. Denes, and U. Dahmen, Microsc. Microanal. **14**, 469 (2008).
[12] M. Haider, H. Müller, S. Uhlemann, J. Zach, U. Loebau, and R. Hoeschen, Ultramicroscopy **108**, 167 (2008).
[13] M. A. O'keefe, E. C. Nelson, Y. C. Wang, and A. Thust, Philos. Mag. B **81**, 1861 (2001).
[14] F. Gao, D. J. Bacon, and S. Newall, Philos. Mag. Lett. **77**, 229 (1998).
[15] F. Gao and D. J. Bacon, Philos. Mag. A **67**, 289 (1993).
[16] G. Lucas and L. Pizzagalli, Nucl. Instrum. Methods Phys. Res. B **229**, 359 (2005).
[17] G. Kresse and J. Hafner, Phys. Rev. B **47**, 558 (1993); **49**, 14251 (1994).
[18] G. Kresse and J. Furthmüller, Comput. Mater. Sci. **6**, 15 (1996).
[19] G. Kresse and J. Furthmüller, Phys. Rev. B **54**, 11169 (1996).
[20] J. P. Perdew, K. Burke, and M. Ernzerhof, Phys. Rev. Lett. **77**, 3865 (1996).
[21] P. E. Blöchl, Phys. Rev. B **50**, 17953 (1994).
[22] G. Kresse and D. Joubert, Phys. Rev. B **59**, 1758 (1999).
[23] R. Kilaas, in *Proceedings of the 45th Annual Meeting of the Electron Microscopy Society of America*, Baltimore, MD (San Francisco Press, San Francisco, 1987), edited by G. W. Bailey, pp. 66–67.
[24] W. A. McKinley and H. Feshbach, Phys. Rev. **74**, 1759 (1948).
[25] J. W. Corbett, in *Solid State Physics*, edited by F. Seitz and D. Turnbull (Academic, New York, 1966).
[26] P. Jung, Phys. Rev. B **23**, 664 (1981).
[27] Z. Chowdhuri, G. L. Hansen, V. Jane, C. D. Keith, W. M. Lozowski, W. M. Snow, M. S. Dewey, D. M. Gilliam, G. L. Greene, J. S. Nico, A. K. Thompson, and F. E. Wietfeldt, Rev. Sci. Instrum. **74**, 4280 (2003).